Physics in Medicine & Biology

IPEM
Institute of Physics and
Engineering in Medicine

PAPER

Calculation of the DNA damage yield and relative biological effectiveness in boron neutron capture therapy via the Monte Carlo track structure simulation

Yang Han[1,2], Changran Geng[1] , Yuanhao Liu[1,3], Renyao Wu[1], Mingzhu Li[1], Chenxi Yu[1], Saverio Altieri[2,4] and Xiaobin Tang[1]

[1] Department of Nuclear Science and Technology, Nanjing University of Aeronautics and Astronautics, Nanjing, People's Republic of China
[2] Department of Physics, University of Pavia, Pavia, Italy
[3] Neuboron Medtech. Ltd, Nanjing, People's Republic of China
[4] Istituto Nazionale di Fisica Nucleare (INFN), the section of Pavia, Pavia, Italy

E-mail: gengchr@nuaa.edu.cn and liuyuanhao@nuaa.edu.cn

Abstract

Objective. Boron neutron capture therapy (BNCT) is an advanced cellular-level hadron therapy that has exhibited remarkable therapeutic efficacy in the treatment of locally invasive malignancies. Despite its clinical success, the intricate nature of relative biological effectiveness (RBE) and mechanisms responsible for DNA damage remains elusive. This work aims to quantify the RBE of compound particles (i.e. alpha and lithium) in BNCT based on the calculation of DNA damage yields via the Monte Carlo track structure (MCTS) simulation. *Approach.* The TOPAS-nBio toolkit was employed to conduct MCTS simulations. The calculations encompassed four steps: determination of the angle and energy spectra on the nuclear membrane, quantification of the database containing DNA damage yields for ions with specific angle and energy, accumulation of the database and spectra to obtain the DNA damage yields of compound particles, and calculation of the RBE by comparison yields of double-strand break (DSB) with the reference gamma-ray. Furthermore, the impact of cell size and microscopic boron distribution was thoroughly discussed. *Main results.* The DSB yields induced by compound particles in three types of spherical cells (radius equal to 10, 8, and 6 μm) were found to be 13.28, 17.34, 22.15 Gy Gbp^{-1} for boronophenylalanine (BPA), and 1.07, 3.45, 8.32 Gy Gbp^{-1} for sodium borocaptate (BSH). The corresponding DSB-based RBE values were determined to be 1.90, 2.48, 3.16 for BPA and 0.15, 0.49, 1.19 for BSH. The calculated DSB-based RBE showed agreement with experimentally values of compound biological effectiveness for melanoma and gliosarcoma. Besides, the DNA damage yield and DSB-based RBE value exhibited an increasing trend as the cell radius decreased. The impact of the boron concentration ratio on RBE diminished once the drug enrichment surpasses a certain threshold. *Significance.* This work is potential to provide valuable guidance for accurate biological-weighted dose evaluation in BNCT.

1. Introduction

Boron neutron capture therapy (BNCT) is one kind of cancer-selective radiotherapy that leverages the large neutron capture cross sections of ^{10}B and cancer-targeting drugs, enabling BNCT to be one of the most effective therapeutic modalities for locally invasive malignancies (Barth *et al* 2018, Dymova *et al* 2020). The primary dose contribution in BNCT arises from the boron neutron capture reaction $n(^{10}\text{B},\alpha)^7\text{Li}$, which generates high LET charged particles (i.e. alpha and lithium particles) and causes the high relative biological effectiveness (RBE) (Hopewell *et al* 2011). A simplified concept of compound biological effectiveness (CBE) is commonly used to describe the RBE of the boron dose fraction, which combines the effect of alpha and lithium particles

(Fukuda 2021). However, this value is significantly influenced by factors such as the microscopic boron distribution and the specific cell line involved. Considering these discrepancies, it becomes essential to trace the origin of RBE back to the fundamental principles.

As emphasized in the review paper conducted by Nikjoo *et al* it will be a major scientific achievement if we can link mechanistically the stages between the initial radiation-induced DNA damage (Nikjoo *et al* 2016). Recent years, many researchers reported their nanoscale Monte Carlo simulation code to analyze the radiation-induced DNA damage for different radiotherapy modalities, including photon, electron, proton, and carbon ion radiotherapy (Chatzipapas *et al* 2020, Kyriakou *et al* 2022). Some cases have established interesting relationships between the DNA damage yield and RBE, which can potentially be applied to predict the radiation response (Kirkby *et al* 2013, Tajik *et al* 2015, Stewart 2018, Montgomery *et al* 2021, Small *et al* 2021, Manalad *et al* 2023). However, Monte Carlo simulations for DNA damage calculation are scarce in BNCT (Qi *et al* 2021). Additionally, the presence of inhomogeneous microscopic boron distribution in BNCT renders DNA damage calculation more complex compared to traditional radiotherapy modalities (Wittig *et al* 2008, Sato *et al* 2018).

Detailed descriptions of the processes involved in the interactions between radiation and material at the nanoscale are key to investigating the radiation-induced DNA damage (Bertolet *et al* 2022). Monte Carlo track structure (MCTS) simulation is a powerful tool for non-empirical particle transport at this scale, which relies on the differential cross section database (Chatzipapas *et al* 2020, D-Kondo *et al* 2021). Several MCTS codes, such as NOREC, PARTRAC, Geant4-DNA, and Phits-KURBUC, have been developed (Chatzipapas *et al* 2020). Among them, Geant4-DNA is the first toolkit made available for open access to the community (Incerti *et al* 2010a, 2010b, Bernal *et al* 2015, Incerti *et al* 2018). However, for heavy ions, Geant4-DNA currently only supports particles with energies higher than 0.5 MeV u^{-1}, limiting its applicability in BNCT, where lithium is emitted with lower energy (i.e. 0.84 or 1.02 MeV).

In previous work, we calculated and verified the new cross sections of lithium by comparing the range and stopping power with data from ICRU 73 (Sigmund *et al* 2009), enabling the accurate MCTS simulation for all charged particles involved in BNCT (Han *et al* 2023). The objective of this study is to quantify the RBE value for compound particles in BNCT based on the calculation of DNA damage yields via the MCTS simulation. To achieve this, TOPAS-nBio 1.0 (Schuemann *et al* 2019), an extension to the Monte Carlo toolkit TOPAS 3.7.0 which wraps and extends the Geant4 10.06.p03, was employed to conduct the MCTS simulation. A previously established physicochemical model, along with a full nuclear model (radius equal to 4.65 μm) with fractal DNA, was utilized in this study. The calculation encompassed four distinct steps. Particle transport outside and inside the cell nucleus was separated, and the overall DNA damage yields of the compound particles (i.e. alpha and lithium) were obtained by accumulation. Subsequently, RBE was determined in comparison with the reference gamma radiation. Besides, the impact of cell size and microscopic boron distribution was thoroughly discussed.
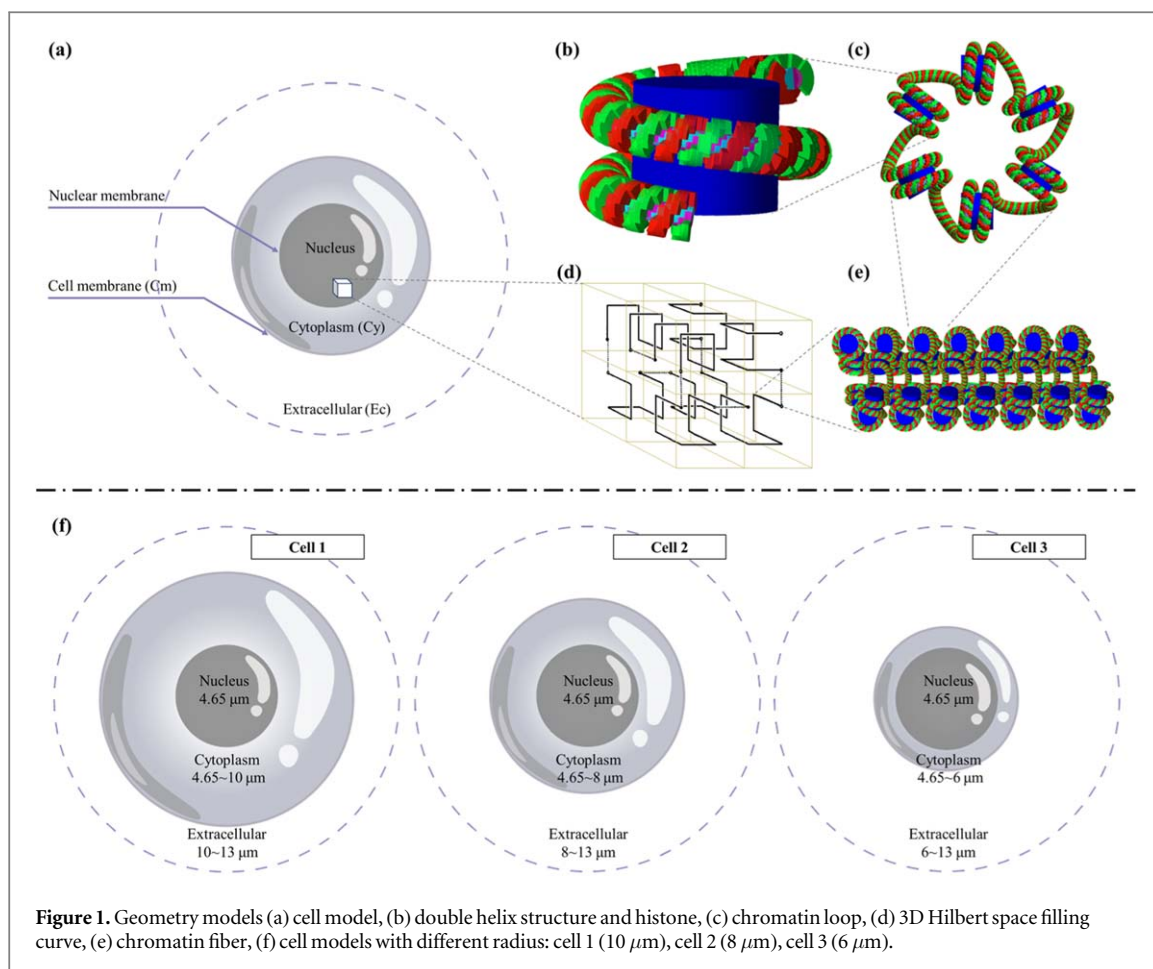
2. Materials and methods

2.1. Geometry models

The investigation of DNA damage based on the MCTS simulation typically relies on the geometric modeling of cell, nucleus, and DNA subcomponents. In this study, we employed a spherical structure implemented in TOPAS-nBio to represent the cell geometry, as illustrated in figure 1(a). The utilization of spherical cells has been widely recognized as an effective approach for modeling various realistic cell types, such as suspended lymphocytes (Rosenbluth *et al* 2006) and hepatoma cells (Laurent *et al* 2012). The comprehensive geometry model encompassed the extracellular space (Ec), cell membrane (Cm), cytoplasm (Cy), and nucleus. The radii of spherical cells were set to 10 (cell 1), 8 (cell 2), and 6 (cell 3) μm, as depicted in figure 1(f). The nucleus located at the cell center had a radius of 4.65 μm (McNamara *et al* 2018). In human cells, the nucleus has a hierarchical structure from chromosome territories, chromatin fibers, chromatin loops, nucleosomes down to the DNA double helix structure, as shown in figures 1(b)–(e). This work used a previously developed full nuclear model (i.e. 'TsNucleus'), which incorporates these biological structures at different scales by utilizing fractally folded DNA (McNamara *et al* 2018). Additionally, the 'QuarterCylinder' model was employed to describe the double helix structure. The nucleus contains 23 chromosome territories and 6.078 Giga base pairs (Gbp) of DNA, with each fiber comprising 15 150 Bp. Detailed parameters of the nuclear and DNA structure can be found on the website: https://topas-nbio.readthedocs.io/en/latest/Geometries/Nucleus.html.

2.2. Physics and chemistry models

Geant4-DNA currently exhibits limitations in accurate particle transport for ions with energy below 0.5 MeV u^{-1} because of the neglect of charge exchange and excitation processes (Incerti *et al* 2014), which pose challenges when using this MCTS toolkit for lithium transport in BNCT. According to previous work, we adopted the modified cross sections of lithium derived by the effective charge cross section scalation method and

Figure 1. Geometry models (a) cell model, (b) double helix structure and histone, (c) chromatin loop, (d) 3D Hilbert space filling curve, (e) chromatin fiber, (f) cell models with different radius: cell 1 (10 μm), cell 2 (8 μm), cell 3 (6 μm).

Table 1. Parameters in physics and chemistry models (Nikjoo *et al* 1997, Moeini *et al* 2020).

Parameter	Value
Lower linear probability threshold (E_{lower})	5 eV
Higher linear probability threshold (E_{higher})	37.5 eV
Probability for ·OH to cause damage (P_{OH})	13%
Chemical stage time end (T_{chem})	1.0 ns
Time step resolution (dt)	0.5 ps

phenomenological double-parameter modification (Han *et al* 2023). For the other particles in BNCT (i.e. electron, photon, proton, and alpha), the same parameters as 'G4EmDNAphysics_option2' were chosen in our physics model 'TsEmDNAPhysics'. Besides, the chemistry model employed in this work was designated as 'TsEmDNAChemistry' (Ramos-Mendez *et al* 2018). The crucial parameters associated with these models can be found in table 1 (Nikjoo *et al* 1997, Moeini *et al* 2020). To quantify direct damage, a linear probability threshold was utilized, whereby the probability of inducing a strand break (SB) was set to 0 before 5 eV, increased linearly within the 5–37.5 eV range, and remained constant at 1 thereafter. Furthermore, an interaction between hydroxyl (i.e. ·OH) and sugar-phosphate exhibited a 13% probability of generating a SB. The chemical stage duration was set as 1 ns (approximately the lifetime of ·OH radicals in cells) (Hall and Giaccia 2006), and the time resolution was set as 0.5 ps. Additionally, histones were set as free radical scavengers.

2.3. DNA damage yields calculation and RBE evaluation

In conventional DNA damage simulations for external radiotherapy, it is customary to employ an isotropic source that is uniformly distributed throughout the volume (e.g. electrons generated during x-ray radiotherapy) or a parallel beam source where primary particles are emitted from a fixed direction (e.g. proton and carbon ion radiotherapy). However, the presence of heterogeneous microscopic boron distribution in BNCT necessitates a

Figure 2. Schematic diagram of the MCTS simulation and analysis process.
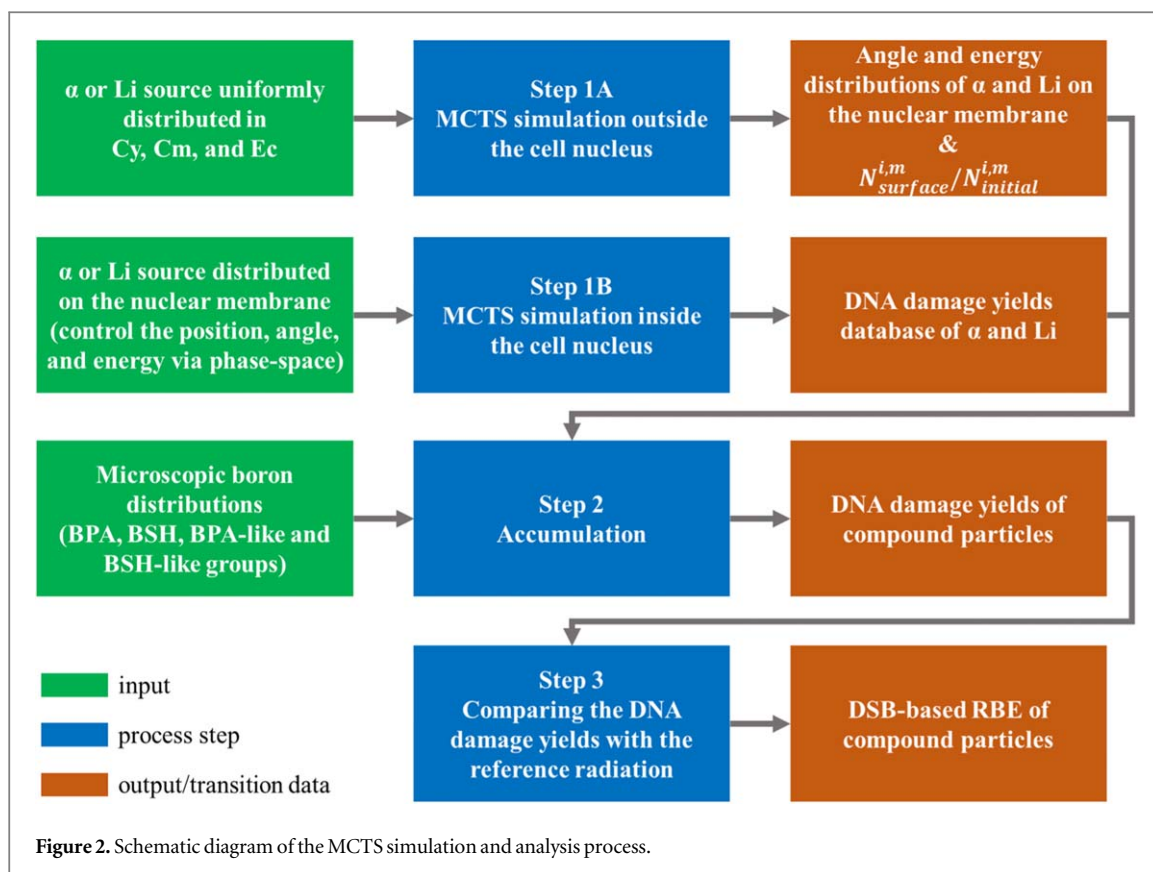
different simulation setup compared to previous cases. To enhance code reusability, the calculations encompassed four steps, as depicted in figure 2.
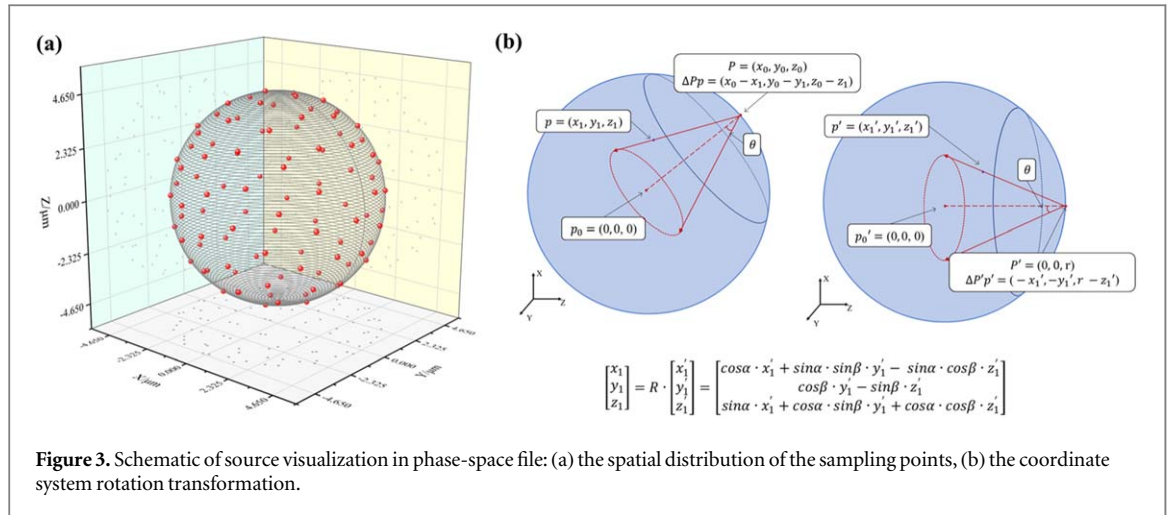
2.3.1. Step 1A: MCTS simulation outside the cell nucleus

In this step, the primary objective was to obtain the angle and energy spectra of alpha and lithium particles on the nuclear membrane when utilizing different isotropic and volumetric sources which represent the heterogeneous drug distribution. The angle in question represented the angle formed between the particle momentum and the normal vector to the nuclear membrane. In this study, we specifically focused on two clinically employed boron drugs, boronophenylalanine (BPA) and sodium borocaptate (BSH). BPA has similar properties to tyrosine, enabling its transport across the cell membrane via amino acid transport proteins and subsequent enrichment in the cytoplasm (Wittig *et al* 2000, Sato *et al* 2018). On the other hand, BSH is known to face challenges in crossing the cell membrane due to the absence of associated transport passage (Michiue *et al* 2014). Considering these characteristics, three source conditions of alpha and lithium particles, i.e. isotopic source uniformly distributed in the cytoplasm (Cy), cell membrane (Cm), and extracellular space (Ec), were employed in this step. To ensure accurate scoring and analysis, we established an energy bin size of 0.001 MeV and an angle bin size of 0.018 degrees.

2.3.2. Step 1B: MCTS simulation inside the cell nucleus

In this step, we aimed to build a database describing the relationship between the DNA damage yields and the specific angle and energy of particles emitted on the nuclear membrane. To achieve this, we need to control the primary particle information in each phase-space source file. The phase-space files contain information including particle position (x, y, z), momentum direction ($\cos x$, $\cos y$, $\cos z$), energy, particle type (PDG format), and weight. A kinetic iterative method was utilized to make sure that all particles written in the phase-space file were uniformly distributed on the nuclear membrane, as shown in figure 3(a). In addition, to ensure a consistent angle in each phase-space file, we employed a coordinate system rotation transformation, thereby assigning a specific momentum to each sampling point, as shown in figure 3(b). To explore a wide range of angles, we selected specific values for different phase-space files, including 0, 15, 30, 45, 60, 75, 80, 85 and 90 degrees. Furthermore, in order to examine various energy levels, the particle energies in different phase-space files were set to 0.1, 0.2, 0.3, 0.4, 0.5, 0.6, 0.7, 0.8, 0.9, 1.0, 1.2, 1.4, 1.6, 1.8 MeV for alpha, and 0.1, 0.2, 0.3, 0.4, 0.5, 0.6, 0.7, 0.8, 0.9, 1.0 MeV for lithium.

Figure 3. Schematic of source visualization in phase-space file: (a) the spatial distribution of the sampling points, (b) the coordinate system rotation transformation.

Radiation-induced DNA damage is closely associated with the occurrence of DNA breaks, which can be attributed to either direct or indirect actions. In particular, damage to the DNA backbone is assumed to result in strand breaks. In direct action, DNA damage arises from the direct transfer of radiation energy to DNA molecules. On the other hand, indirect action involves the interaction between reactive chemical species and DNA molecules. In this work, DNA damage was categorized as single-strand break (SSB) and double-strand break (DSB). The distance between two damage sites in DSB did not exceed 10 Bp (McNamara *et al* 2017). Besides, the direct, indirect, and hybrid damage (e.g. a hybrid DSB site consisting of one SB from direct damage and another SB from indirect damage) were considered. Additionally, we assumed that each radiation track acted independently of others. According to the recommendations provided in the published work, the effect of intertrack synergistic effects needs to be considered only at the dose up to 600 Gy for heavy ions (Kreipl *et al* 2009).

We utilized the unit of '/event/nucleus' for assessing DNA damage yields, as opposed to the commonly used unit of '/Gy/Gbp'. This distinction arises due to the statistical inhomogeneity of boron dose at the cellular or subcellular scale in BNCT, considering the specific microscopic distribution of boron and the short range of secondary particles. In essence, when delivering one Gy of the macroscopic dose to tissue or tumor, the dose within the cell nucleus will not be one Gy.

2.3.3. Step 2: accumulation

To obtain the DNA damage yields for particles with complicated angle (θ) and energy (E) spectra ($\overline{Y}_l^{i,m}|_{\text{perevent}}$), the previously calculated spectra and database were weighted according to the following formula:

$$\overline{Y}_l^{i,m}|_{\text{perevent}} = \sum_{\theta,E} Q_{\theta,E}^{i,m} \cdot Y_{l,\theta,E}^i |_{\text{perevent}}, \tag{1}$$

where $Y_{l,\theta,E}^{i,m}|_{\text{perevent}}$ represents the DNA damage yield obtained in step 1B, l refers to the DNA damage type (i.e. SSB and DSB), i refers to the particle type (i.e. alpha and lithium particles), m refers to the source condition (i.e. Cy, Cm, and Ec), $Q_{\theta,E}^{i,m}$ denotes the particle frequency calculated in step 1A. Before the weighting process, we employed a 2D cubic interpolation to ensure the correspondence of $Q_{\theta,E}^{i,m}$ and $Y_{l,\theta,E}^{i,m}|_{\text{perevent}}$.

In realistic BNCT scenarios, it is crucial to consider the intricate distribution of boron drugs within the cellular environment. Thus, the DNA damage yields calculated by equation (1) need to be appropriately weighted taking into account the different microscopic boron distributions. In addition, the assessment of the combined effect of alpha and lithium particles is essential to align with the concept of CBE in clinical. Besides, under the assumption that the current clinically used boron drugs are mainly enriched outside the nucleus, alpha and lithium particles can be considered as independent particles. This is due to the fact that the same capture reaction generates two charged particles with opposing momenta, and at most, only one particle can enter the nucleus. Consequently, we can calculate the DNA damage yield of the compound particles ($\overline{Y}_l^n|_{\text{perevent}}$) in BNCT by the following formula:

$$\overline{Y}_l^n|_{\text{perevent}} = \sum_{i,m} \frac{N_{\text{surface}}^{i,m}}{N_{\text{initial}}^{i,m}} \cdot W^{n,m} \cdot \overline{Y}_l^{i,m}|_{\text{perevent}}, \tag{2}$$

where n refers to the microscopic boron distribution group, $N_{\text{initial}}^{i,m}$ represents the number of primary particles emitted in step 1A, $N_{\text{surface}}^{i,m}$ represents the number of particles reaching the nucleus membrane in step 1A, $W^{n,m}$ denotes the microscopic boron element ratio. The boron element ratio refers to the percentage of the number of [10]B atoms in each condition (Cy, Cm, Ec) relative to the total number of [10]B atoms, which is determined by the

Table 2. Microscopic boron element ratio.

| Cell model | Boron drug | $W^{n,m}$ | | |
		Cytoplasm (Cy)	Cell membrane (Cm)	Extracellular (Ec)
Cell 1	BPA	0.73	0	0.27
	BSH	0	0.42	0.58
Cell 2	BPA	0.49	0	0.51
	BSH	0	0.21	0.79
Cell 3	BPA	0.26	0	0.74
	BSH	0	0.09	0.91

intracellular/extracellular boron concentration ratios. The reference boron concentration ratio in this study is taken from the experimental data for melanoma cells, which is approximately 3.2 for BPA and 0.86 for BSH (Sato *et al* 2018). The corresponding $W^{n,m}$ values calculated by the cell volumes and boron concentrations are listed in table 2. The calculation formulas are shown in the appendix.

2.3.4. Step 3: DSB-based RBE calculation
In the final step, we computed the DSB-based RBE values (RBE_{DSB}) by comparing DSB yields induced by the compound particles in BNCT with those from the reference radiation at the same absorbed dose. It is important to note that the conventional RBE, which refers to the ratio of absorbed doses required by the tested radiation and the reference radiation to achieve the same biological endpoint, carries a different meaning. However, numerous investigations aiming to establish a connection between nanoscopic DNA damage and the traditional RBE have adopted the DSB-based RBE as a metric to evaluate the potential biological outcomes, considering the challenging repair process associated with DSB (Kirkby *et al* 2013, Tajik *et al* 2015, Stewart 2018, Montgomery *et al* 2021, Small *et al* 2021, Manalad *et al* 2023).

In this study, we utilized ^{137}Cs gamma-ray as the reference radiation, which provides a simple energy spectrum and induces DNA damage yields essentially equivalent to the commonly used ^{60}Co gamma-ray or 250 kVp x-ray (Hsiao and Stewart 2008). Photon transport is inefficient at the micron or nanometer scale, so we approximated the simulation using the secondary electron spectrum of ^{137}Cs. The isotropic electron source was uniformly distributed throughout the cell volume. To facilitate a comparison of DNA damage yields with the reference gamma-ray using a standardized framework, we performed a unit transformation from '/event/nucleus' to '/Gy/Gbp' when calculating the DSB-based RBE. The DSB-based RBE calculation approach can be described by the following formula:

$$\text{RBE}_{\text{DSB}}^{n} = \frac{Q \cdot \overline{Y}_{\text{DSB}}^{n}|_{\text{perevent}}}{M \cdot \overline{Y}_{\text{DSB}}^{\text{gamma}}|_{\text{perGy}}}, \tag{3}$$

where $\overline{Y}_{\text{DSB}}^{\text{gamma}}|_{\text{perGy}}$ represents the DSB yield induced by the reference gamma-ray, M refers to the number of base pair in the nucleus, Q is the dose-event transformation factor calculated by the following expression:

$$Q = \frac{\rho \cdot V}{E}, \tag{4}$$

where ρ is the density of water, V is the volume of the sphere with 13 μm radius in this study, E is the average energy deposition per boron neutron capture reaction.

3. Results and discussion

3.1. Angle and energy distributions of alpha and lithium particles on the nuclear membrane
Figure 4 illustrates the angle distributions of alpha and lithium particles on the nuclear membrane under three source conditions (i.e. Cy, Cm, and Ec). Different rows in figure 4 correspond to results calculated with different cell radii, i.e. cell 1 (10 μm), cell 2 (8 μm), and cell 3 (6 μm). Due to the short range, it is difficult for lithium to penetrate the cytoplasm of cell 1 and cell 2 when using Cm and Ec source conditions. Therefore, figures 4(b) and (d) only present the results under the Cy condition. The particle angles on the nuclear membrane are concentrated between 20 and 70 degrees. Notably, the angle distributions differ depending on the source condition and cell size. Besides, as the source is located farther away from the nucleus, the particle angles reaching the nuclear membrane become smaller.

Figure 5 displays the energy spectra of alpha and lithium particles on the nuclear membrane under three source conditions (i.e. Cy, Cm, and Ec). Different rows in figure 5 correspond to results calculated with different cell radii, i.e. cell 1 (10 μm), cell 2 (8 μm), and cell 3 (6 μm). Due to the short range, it is difficult for lithium to
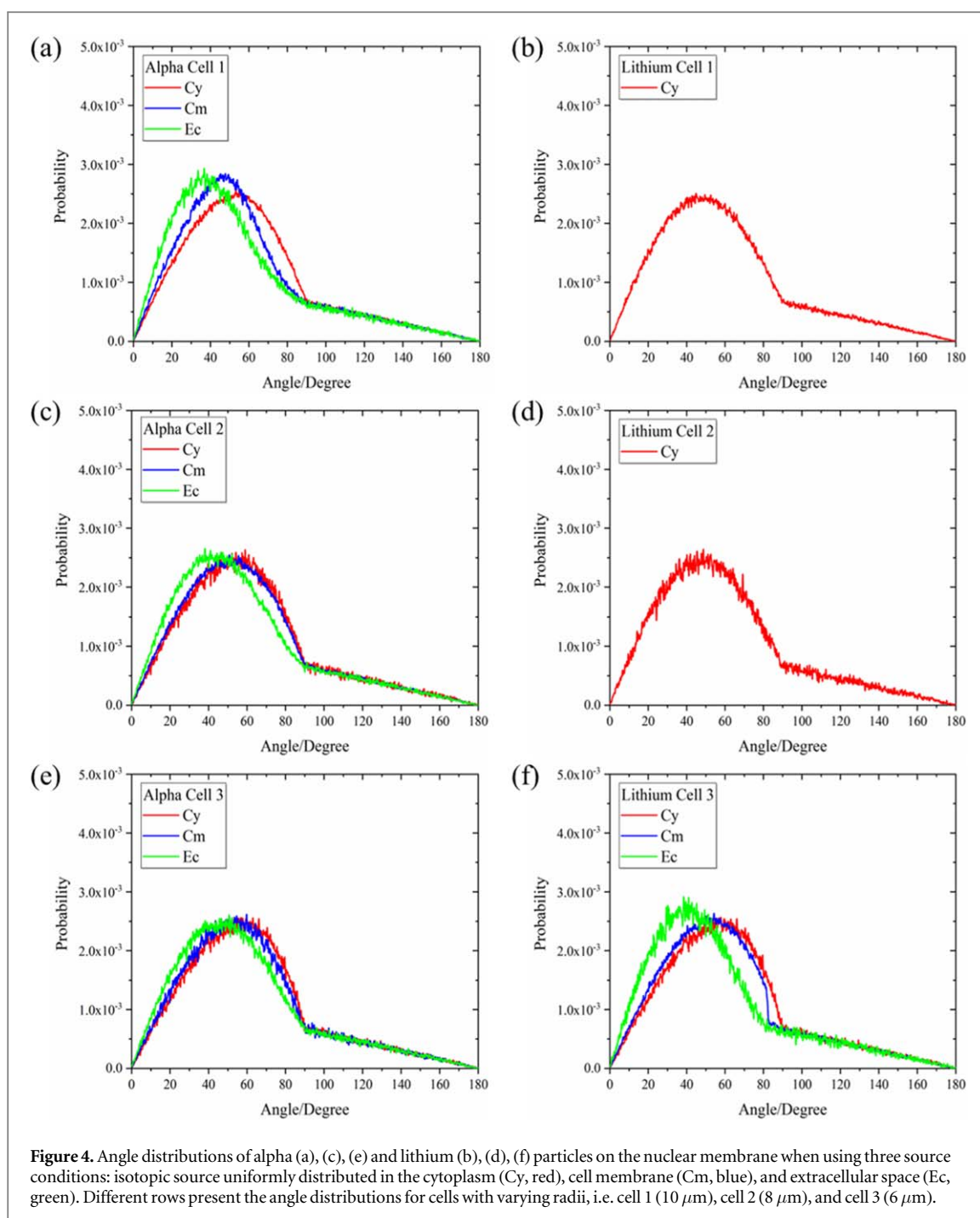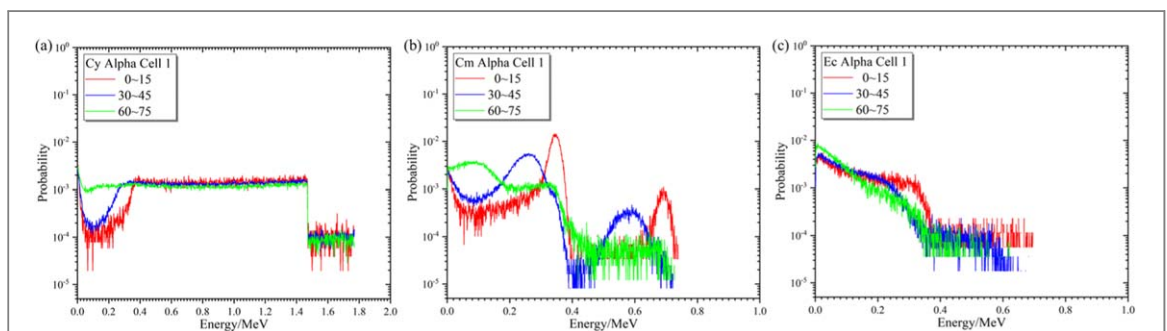
Figure 4. Angle distributions of alpha (a), (c), (e) and lithium (b), (d), (f) particles on the nuclear membrane when using three source conditions: isotopic source uniformly distributed in the cytoplasm (Cy, red), cell membrane (Cm, blue), and extracellular space (Ec, green). Different rows present the angle distributions for cells with varying radii, i.e. cell 1 (10 μm), cell 2 (8 μm), and cell 3 (6 μm).

penetrate the cytoplasm of cell 1 and cell 2 when using Cm and Ec source conditions. Therefore, figures 5(b) and (d) only present the results under the Cy condition. Notably, the energy spectra exhibit substantial variations among different groups. Specifically, under the Cy source condition, the energy spectra of alpha particles show distinct boundaries at 1.47 and 1.77 MeV, whereas for lithium, the boundaries are at 0.84 and 1.02 MeV, corresponding to the two reaction channels of the boron neutron capture reaction. Similarly, two boundaries with lower energy can also be observed when utilizing the Cm source condition. Besides, increasing cell size can lead to a more significant discrepancy in the energy spectrum represented in the Cy (red lines) and Cm (blue lines) cases. Furthermore, the particle probability demonstrates a continuous decreasing trend as energy increases when using the Ec source condition.

Figure 6 depicts the energy spectra of alpha particles on the nuclear membrane of cell 1 within different angle ranges, considering three distinct source conditions (i.e. Cy, Cm, and Ec). Notably, the energy spectra exhibit notable variations across different angle ranges, even when the source and cell model conditions are kept constant. Specifically, a higher probability of particles in the low-energy region is observed with larger angle ranges. These findings illustrate the complexity of the particle angle and energy spectrum on the nuclear
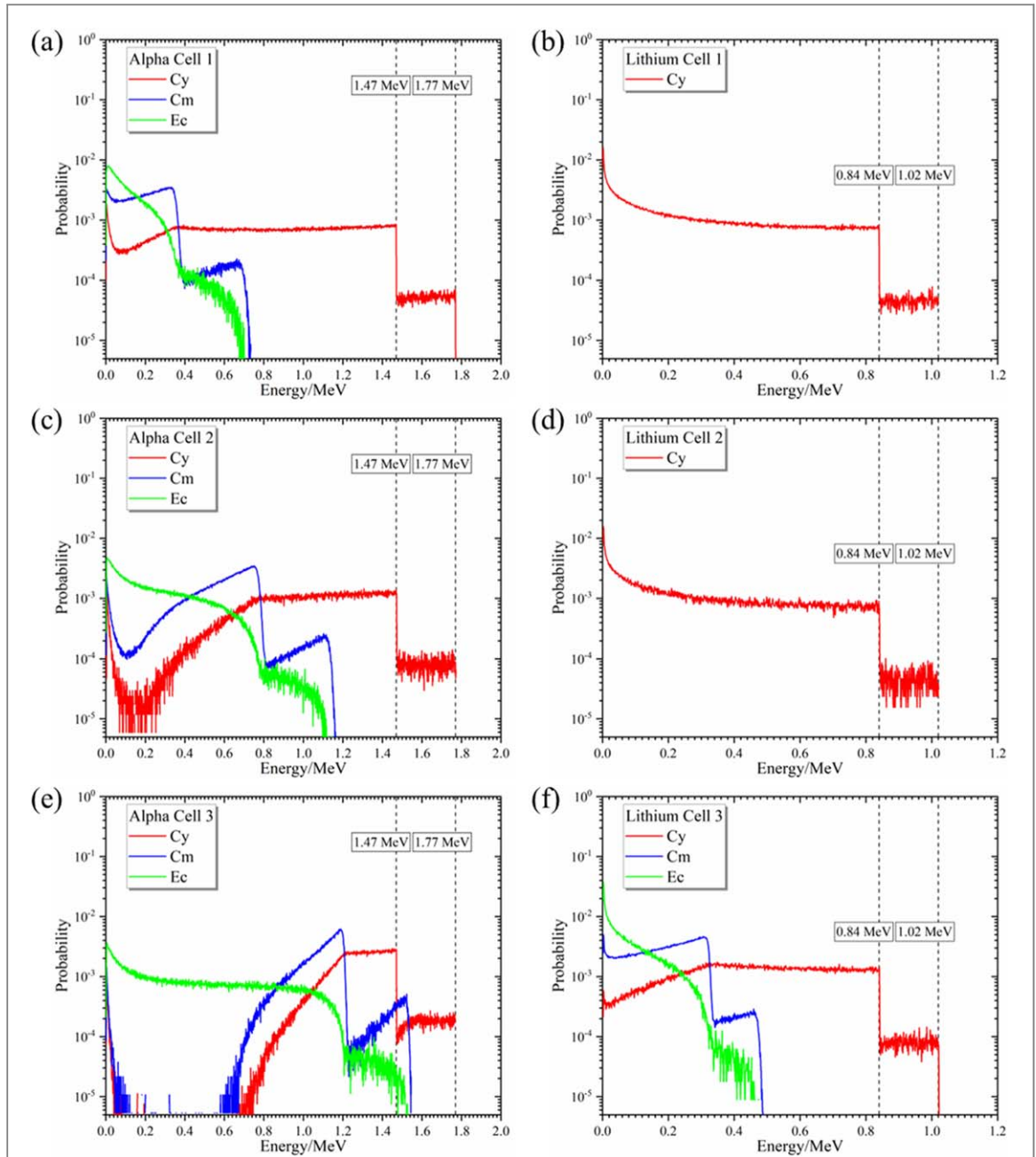
Figure 5. Energy spectra of alpha (a), (c), (e) and lithium (b), (d), (f) particles on the nuclear membrane when using three source conditions: isotopic source uniformly distributed in the cytoplasm (Cy, red), cell membrane (Cm, blue), and extracellular space (Ec, green). Different rows present the energy spectra for cells with varying radii, i.e. cell 1 (10 μm), cell 2 (8 μm), and cell 3 (6 μm).

Figure 6. Energy spectra of alpha particles on the nuclear membrane of cell 1 within different angle ranges when using three source conditions: isotopic source uniformly distributed in the cytoplasm (a), cell membrane (b), and extracellular space (c). Various colors represent different angle ranges, i.e. 0–15 degrees (red), 30–45 degrees (blue), and 60–75 degrees (green).

Table 3. $N_{\text{surface}}^{i,m}/N_{\text{initial}}^{i,m}$ values for three source conditions and cell models.

Cell model (cell radius)	Alpha			Lithium		
	Cy	Cm	Ec	Cy	Cm	Ec
Cell 1 (10 μm)	0.1183	0.0578	0.0249	0.0586	0	0
Cell 2 (8 μm)	0.1683	0.0981	0.0393	0.1283	0	0
Cell 3 (6 μm)	0.2655	0.1860	0.0531	0.2628	0.1792	0.1124

membrane in the BNCT environment. Therefore, the conventional source settings utilized for DNA damage simulations in external irradiation radiotherapy, such as homogeneous volumetric or planar sources, inadequately represent the distribution of radiation particle sources in BNCT.

In addition, the $N_{\text{surface}}^{i,m}/N_{\text{initial}}^{i,m}$ values are listed in table 3, which describe the probability of particles reaching the cell membrane from the emission position. There is a larger $N_{\text{surface}}^{i,m}/N_{\text{initial}}^{i,m}$ value for the Cy group compared to the Cm and Ec groups, in virtue of its particle emission positions closer to the nuclear membrane. Besides, the larger the cell radius, the smaller the $N_{\text{surface}}^{i,m}/N_{\text{initial}}^{i,m}$ value when using the same source condition.

3.2. DNA damage database of mono-energetic and mono-angular alpha and lithium particles

Figure 7 presents the database of DNA damage yields introduced by mono-energetic and mono-angular alpha and lithium particles inside the cell nucleus. The corresponding results for the DSB yield of alpha, SSB yield of alpha, DSB yield of lithium, and SSB yield of lithium are labeled as (a), (b), (c) and (d) in figure 7, respectively. The left column of the figure displays the trend of DNA damage yield with respect to particle energy, while the right column depicts the yield trend with particle emission angle on the nuclear membrane. The DNA damage yields were measured in units of /event/nucleus, where each event represents one primary particle track. Our empirical observations demonstrated a noteworthy correlation, indicating that the relationship between damage yield and particle energy follows a linear pattern for the small angle groups (i.e. 0, 15, 30 and 45 degrees). However, in the large angle groups (i.e. 60, 75, 80, 85 and 90 degrees), we discovered a characteristic behavior: once a certain threshold is reached, the DNA damage yield ceases to rise despite further increments in incident particle energy. The main reason is that particles with higher energy can penetrate the cell nucleus along the path of the chord length. Furthermore, we found a conspicuous trend wherein the DNA damage yield remains relatively stable during the initial stages and rapidly declines as the emission angle increases.

3.3. DNA damage yields and DSB-based RBE of the reference gamma-ray and compound particles for BPA and BSH
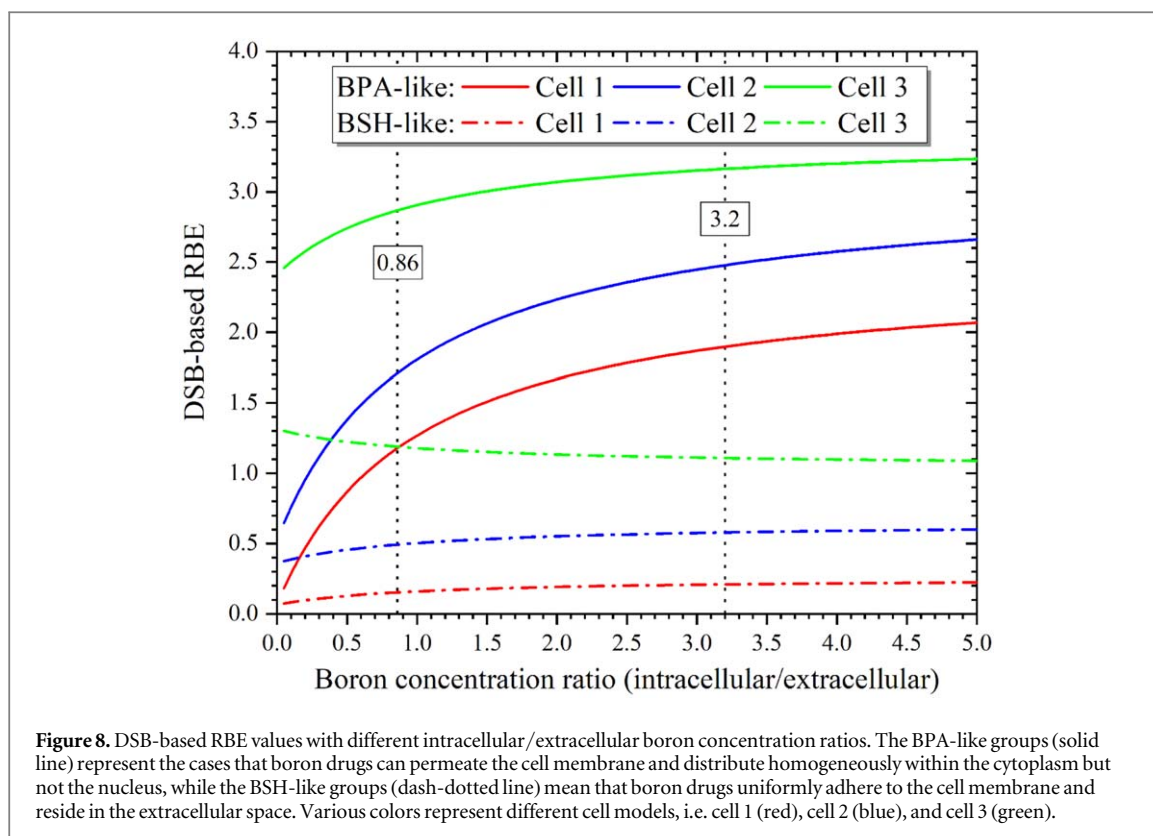
Table 4 presents the DNA damage yields (/Gy/Gbp) of compound particles in BNCT compared to those induced by the reference gamma-ray (i.e. ^{137}Cs). The corresponding DSB-based RBE values for three cell models were calculated by equation (3). The DSB yields induced by compound particles in three cell types (i.e. cell 1, cell 2, and cell 3) were quantified as 13.28, 17.34, 22.15 Gy Gbp^{-1} for BPA, and 1.07, 3.45, 8.32 Gy Gbp^{-1} for BSH, respectively. The corresponding DSB-based RBE values were determined to be 1.90, 2.48, 3.16 for BPA, and 0.15, 0.49, 1.19 for BSH. Notably, the DSB-based RBE value for cell 2 (with a radius of 8 μm) closely approximates the CBE value observed in melanoma cells (with a radius of approximately 8.7 μm) (Ochalek *et al* 1988). Similarly, the DSB-based RBE value for cell 3 (with a radius of 6 μm) exhibits a resemblance to the CBE values observed in ^{9}L-gliosarcoma cells (with a radius ranging from approximately 5.5–7.5 μm) (Rad *et al* 2007). Furthermore, the SSB yield, DSB yields, and DSB-based RBE values of compound particles exhibit an upward trend as the cell radius decreases. This behavior can be attributed to the thinner cytoplasm, the easier for particles to penetrate into the nuclear and introduce DNA damage. Besides, the reason for the discrepancy in RBE values between the two boron distributions is that a substantial portion of the absorbed dose is deposited outside the cell when using BSH, thereby limiting the generation of sufficient DNA damage within the nucleus.

3.4. DSB-based RBE with different microscopic boron concentrations

Considering the variability in pharmacokinetic mechanisms of boron drugs and microenvironment (e.g. oxygenation status and nutritional status) which influence the boron uptake (Masunaga *et al* 2020), the characterization of the microscopic boron distribution across different boron drugs and cell lines is pivotal in assessing the RBE value. In section 3.3, we reported the distinct DSB-based RBE values for the BPA (boron concentration ratio of 3.2) and BSH (boron concentration ratio of 0.86) cases based on experimental data obtained from melanoma cells. In this section, we conducted a more comprehensive investigation to explore the influence of microscopic boron concentration. Specifically, we assumed a BPA-like pattern which followed a similar transport mechanism to BPA, where boron drugs could permeate the cell membrane and distribute
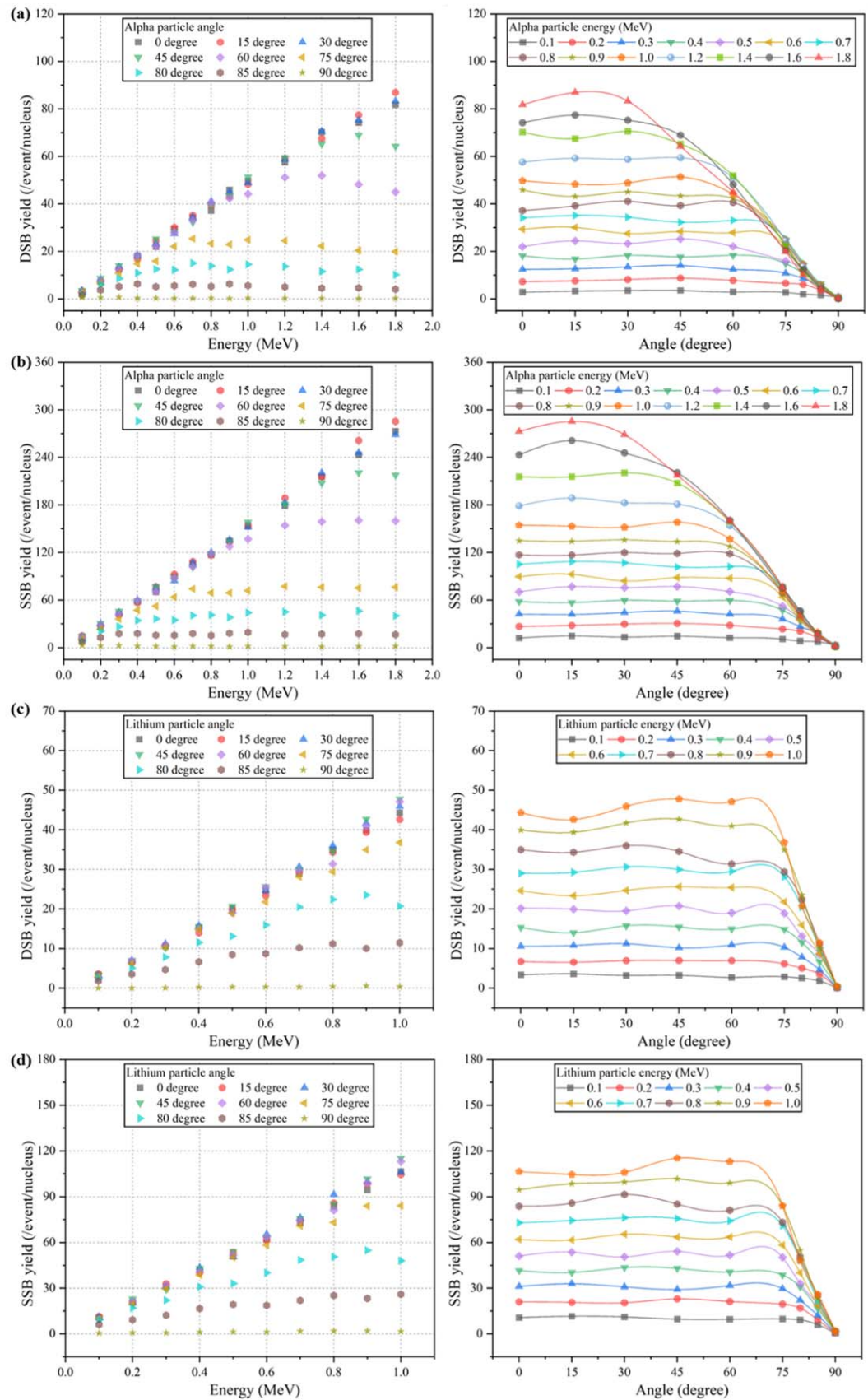
Figure 7. DNA damage database: (a) DSB yield of alpha particles, (b) SSB yield of alpha particles, (c) DSB yield of lithium particles, (d) SSB yield of lithium particles. The left column of the figure showcases the trend of yields with respect to particle energy, while the right column represents the trend of yields with angle.

Figure 8. DSB-based RBE values with different intracellular/extracellular boron concentration ratios. The BPA-like groups (solid line) represent the cases that boron drugs can permeate the cell membrane and distribute homogeneously within the cytoplasm but not the nucleus, while the BSH-like groups (dash-dotted line) mean that boron drugs uniformly adhere to the cell membrane and reside in the extracellular space. Various colors represent different cell models, i.e. cell 1 (red), cell 2 (blue), and cell 3 (green).

Table 4. DNA damage yields and DSB-based RBE values of the reference gamma-ray and compound particles in BNCT.

Groups	DNA damage yields (/Gy/Gbp)		DSB-based RBE (this work) or CBE (reported)
	SSB	DSB	
Gamma (^{137}Cs)	133.3±4.5	7.0±0.1	1
BPA (Cell 1, 10 μm)	40.59	13.28	1.90
BPA (Cell 2, 8 μm)	52.67	17.34	2.48
BPA (Cell 3, 6 μm)	66.90	22.15	3.16
BPA (B-16 melanoma)	—	—	2.3 (Coderre *et al* 1991)
BPA (Green's melanoma)	—	—	2.5 (Hiratsuka *et al* 1989)
BPA (^{9}L-gliosarcoma)	—	—	3.8 (Coderre *et al* 1993)
BSH (Cell 1, 10 μm)	3.71	1.07	0.15
BSH (Cell 2, 8 μm)	10.96	3.45	0.49
BSH (Cell 3, 6 μm)	25.96	8.32	1.19
BSH (^{9}L-gliosarcoma)	—	—	1.2 (Coderre *et al* 1993)

homogeneously within the cytoplasm and extracellular space but not the nucleus. Conversely, a BSH-like pattern was assumed, wherein boron drugs would uniformly adhere to the cell membrane and reside in the extracellular space. The results shown in figure 8 reveal that the DSB-based RBE value of cell 3 exceeds those of cell 2 and cell 1 when using the same boron concentration ratio. This discrepancy can be attributed to the particles' ability to traverse the cytoplasm, as previously elucidated in section 3.3. Besides, except for cell 3 under the BSH condition, the other cases exhibit an increasing trend of the DSB-based RBE value as the boron concentration ratio increases but the gradient slows down until reaching a plateau. This indicates that the impact of the boron concentration ratio on RBE diminishes once the drug enrichment surpasses a certain threshold. In contrast, the curve exhibits an opposite pattern for cell 3 under the BSH condition because of the thin cytoplasm, whereby ions emitted in the extracellular space are able to effectively access the nucleus. Additionally, the BPA-like groups demonstrate higher susceptibility to the effect of the boron concentration ratio compared to the BSH-like groups. The results presented here emphasize the importance to understand the transport passages of boron drugs and develop boron measurement techniques at the cellular or subcellular scale (Probst 1999, Wittig *et al* 2008).

3.5. Applications, limitations, and future directions

This study represents the first attempt to calculate the DNA damage yield and evaluate the RBE value of compound particles in BNCT using the MCTS method. This approach offers a theoretical framework for future investigations aimed at accurately assessing the biological-weighted dose of BNCT in clinical and experimental cases. Nonetheless, it is important to acknowledge that the present study is in its preliminary phase, necessitating further advancements for enhanced applicability. The following items highlight the study's limitations and outline the developing directions:

(1) The cellular model employed in this study assumes a spherical shape, whereas actual cells may exhibit an ellipsoidal (Douglass *et al* 2012, Meylan *et al* 2017) or irregular morphology (Tang *et al* 2021). Hence, further refinement of the cell geometry is valuable in future investigations. Besides, the cell nucleus utilized in this study relies on the built-in nucleus model in Topas-nBio. However, there are variations in the size of nuclei among human cells, and certain cell lines may possess multiple nuclei (Webster *et al* 2009). The investigation of the influence of nuclear morphology on the DNA damage yields in BNCT is crucial.

(2) The classification of DNA damage should be further refined. Because the clustered DNA damage was proven to be always longer-lived or mis-linked, which can ultimately lead to cell death, it is plausible that clustered DSB yield is more closely associated with the CBE value (Incerti *et al* 2016).

(3) The present study focuses on characterizing the early physicochemical processes that occur during radiation interaction and their impact on DNA damage. However, it is essential to explore the biological repair patterns that encompass various repair pathways and molecular mechanisms (Bernal *et al* 2015). Previous research in other radiotherapy modalities has highlighted the involvement of non-homologous end-joining (NHEJ) and homologous recombination repair (HRR) pathways in DSB repair. These repairing processes engage numerous proteins/enzymes, such as γ-H2AX, Rad51, Rad54, Ku70/80, DNA-PKcs, and IV-XRCC4 (Kinashi *et al* 2011, Okumura *et al* 2013, Kondo *et al* 2016, Rodriguez *et al* 2018, Chen *et al* 2019). Nevertheless, the current understanding of the repair mechanisms in BNCT is limited (Maliszewska-Olejniczak *et al* 2021), and further investigations focusing on repair dynamics (e.g. combining DaMaRiS and MEDRAS models) are crucial (McMahon *et al* 2017, Warmenhoven *et al* 2020).

4. Conclusion

This study successfully employed the Monte Carlo track structure method (TOPAS-nBio) to calculate DNA damage yields and evaluate DSB-based RBE values of compound particles in BNCT. The simulation utilized the cross sections of lithium verified in the previous study and a comprehensive nuclear model with fractal DNA filling. The intricate particle environment encountered in BNCT poses challenges to following the traditional DNA damage calculation modalities. A step-by-step calculation method which separates the particle transport outside and inside the nucleus was adapted for this condition. The impact of cell size and microscopic boron distribution was extensively discussed. The calculated DSB-based RBE values showed agreement with experimentally derived CBE values. Besides, the DNA damage yield and DSB-based RBE value exhibited an increasing trend as the cell radius decreased. Furthermore, the impact of the boron concentration ratio on RBE diminishes once the drug enrichment surpasses a certain threshold. This algorithm is expected to provide valuable guidance for precise biological-weighted dose evaluation in BNCT, although further developments are necessary to enhance its reliability in practice.

Acknowledgments

Data availability statement

All data that support the findings of this study are included within the article (and any supplementary information files).

Appendix

The boron element ratio $W^{n,\,m}$ can be determined by the following formulars:

$$\frac{W^{\mathrm{BPA,Cy}} + W^{\mathrm{BPA,Cm}}}{V_{\mathrm{cell}}} : \frac{W^{\mathrm{BPA,Ec}}}{V_{\mathrm{Ec}}} = 3.2$$

$$\frac{W^{\mathrm{BSH,Cy}} + W^{\mathrm{BSH,Cm}}}{V_{\mathrm{cell}}} : \frac{W^{\mathrm{BSH,Ec}}}{V_{\mathrm{Ec}}} = 0.86$$

subjected to:

$$W^{\mathrm{BPA,Cy}} + W^{\mathrm{BPA,Cm}} + W^{\mathrm{BPA,Ec}} = 1$$

$$W^{\mathrm{BSH,Cy}} + W^{\mathrm{BSH,Cm}} + W^{\mathrm{BSH,Ec}} = 1$$

$$W^{\mathrm{BPA,Cm}} = 0$$

$$W^{\mathrm{BSH,Cy}} = 0$$

in which V_{cell} is the volume of cell and V_{Ec} is the volume of the extracellular space. Considering the transportation mechanism of BPA and BSH discussed in section 2.3.1, the values of $W^{\mathrm{BPA,Cm}}$ and $W^{\mathrm{BSH,Cy}}$ were assumed to be zero.

ORCID iDs

Changran Geng ⬤ https://orcid.org/0000-0002-6332-6193
Saverio Altieri ⬤ https://orcid.org/0000-0002-1376-3686
Xiaobin Tang ⬤ https://orcid.org/0000-0003-3308-0468

References

Barth R F, Zhang Z and Liu T 2018 A realistic appraisal of boron neutron capture therapy as a cancer treatment modality *Cancer Commun.* **38** 1–7

Bernal M A *et al* 2015 Track structure modeling in liquid water: a review of the Geant4-DNA very low energy extension of the Geant4 Monte Carlo simulation toolkit *Phys. Med.-Eur. J. Med. Phys.* **31** 861–74

Bertolet A, Ramos-Méndez J, McNamara A, Yoo D, Ingram S, Henthorn N, Warmenhoven J-W, Faddegon B, Merchant M and McMahon S J 2022 Impact of DNA geometry and scoring on Monte Carlo track-structure simulations of initial radiation-induced damage *Radiat. Res.* **198** 207–20

Chatzipapas K P, Papadimitroulas P, Emfietzoglou D, Kalospyros S A, Hada M, Georgakilas A G and Kagadis G C 2020 Ionizing radiation and complex DNA damage: quantifying the radiobiological damage using Monte Carlo simulations *Cancers* **12** 799

Chen K-H, Lai Z-Y, Li D-Y, Lin Y-C, Chou F-I and Chuang Y-J 2019 Analysis of DNA damage responses after boric acid-mediated boron neutron capture therapy in hepatocellular carcinoma *Anticancer Res.* **39** 6661–71

Coderre J, Slatkin D, Micca P and Ciallella J 1991 Boron neutron capture therapy of a murine melanoma with p-boronophenylalanine: dose-response analysis using a morbidity index *Radiat. Res.* **128** 177–85

Coderre J A, Makar M S, Micca P L, Nawrocky M M, Liu H B, Joel D D, Slatkin D N and Amols H I 1993 Derivations of relative biological effectiveness for the high-LET radiations produced during boron neutron capture irradiations of the 9L rat gliosarcoma *in vitro* and *in vivo Int. J. Radiat. Oncol.* ˙ *Biol.* ˙ *Phys.* **27** 1121–9

D-Kondo N *et al* 2021 DNA damage modeled with Geant4-DNA: effects of plasmid DNA conformation and experimental conditions *Phys. Med. Biol.* **66** 245017

Douglass M, Bezak E and Penfold S 2012 Development of a randomized 3D cell model for Monte Carlo microdosimetry simulations *Med. Phys.* **39** 3509–19

Dymova M A, Taskaev S Y, Richter V A and Kuligina E V 2020 Boron neutron capture therapy: current status and future perspectives *Cancer Commun.* **40** 406–21

Fukuda H 2021 Response of normal tissues to boron neutron capture therapy (BNCT) with B-10-borocaptate sodium (BSH) and B-10-paraboronophenylalanine (BPA) *Cells* **10** 2883

Hall E J and Giaccia A J 2006 Radiobiology for the Radiologist *Int. J. Radiat. Oncol.* ˙ *Biol.* ˙ *Phys.* **6** 627

Han Y, Geng C, D-Kondo J N, Li M, Ramos-Méndez J, Altieri S, Liu Y and Tang X 2023 Microdosimetric analysis for boron neutron capture therapy via Monte Carlo track structure simulation with modified lithium cross-sections *Radiat. Phys. Chem.* **209** 110956

Hiratsuka J, Kono M and Mishima Y 1989 RBEs of thermal neutron capture therapy and 10B (n, α) 7Li reaction on melanoma-bearing hamsters *Pigment Cell Res.* **2** 352–5

Hopewell J, Morris G, Schwint A and Coderre J 2011 The radiobiological principles of boron neutron capture therapy: a critical review *Appl. Radiat. Isot.* **69** 1756–9

Hsiao Y and Stewart R D 2008 Monte Carlo simulation of DNA damage induction by x-rays and selected radioisotopes *Phys. Med. Biol.* **53** 233–44

Incerti S, Baldacchino G, Bernal M, Capra R, Champion C, Francis Z, Gueye P, Mantero A, Mascialino B and Moretto P 2010a The Geant4-DNA project *Int. J. Model. Simul. Sci. Comput.* **1** 157–78

Incerti S, Douglass M, Penfold S, Guatelli S and Bezak E 2016 Review of Geant4-DNA applications for micro and nanoscale simulations *Phys. Med.-Eur. J. Med. Phys.* **32** 1187–200

Incerti S, Ivanchenko A, Karamitros M, Mantero A, Moretto P, Tran H, Mascialino B, Champion C, Ivanchenko V and Bernal M 2010b Comparison of GEANT4 very low energy cross section models with experimental data in water *Med. Phys.* **37** 4692–708

Incerti S *et al* 2018 Geant4-DNA example applications for track structure simulations in liquid water: a report from the Geant4-DNA Project *Med. Phys.* **45** E722–39

Incerti S *et al* 2014 Simulating radial dose of ion tracks in liquid water simulated with Geant4-DNA: a comparative study *Nucl. Instrum. Methods Phys. Res.* B **333** 92–8

Kinashi Y, Takahashi S, Kashino G, Okayasu R, Masunaga S, Suzuki M and Ono K 2011 DNA double-strand break induction in Ku80-deficient CHO cells following boron neutron capture reaction *Radiat. Oncol.* **6** 1–8

Kirkby C, Ghasroddashti E, Poirier Y, Tambasco M and Stewart R 2013 RBE of kV CBCT radiation determined by Monte Carlo DNA damage simulations *Phys. Med. Biol.* **58** 5693

Kondo N, Sakurai Y, Hirota Y, Tanaka H, Watanabe T, Nakagawa Y, Narabayashi M, Kinashi Y, Miyatake S-I and Hasegawa M 2016 DNA damage induced by boron neutron capture therapy is partially repaired by DNA ligase IV *Radiat. Environ. Biophys.* **55** 89–94

Kreipl M S, Friedland W and Paretzke H G 2009 Interaction of ion tracks in spatial and temporal proximity *Radiat. Environ. Biophys.* **48** 349–59

Kyriakou I, Sakata D, Tran H N, Perrot Y, Shin W-G, Lampe N, Zein S, Bordage M C, Guatelli S and Villagrasa C 2022 Review of the Geant4-DNA simulation toolkit for radiobiological applications at the cellular and DNA level *Cancers* **14** 35

Laurent T, Murase D, Tsukioka S, Matsuura T, Nagamori S and Oda H 2012 A novel human hepatoma cell line, FLC-4, exhibits highly enhanced liver differentiation functions through the three-dimensional cell shape *J. Cell. Physiol.* **227** 2898–906

Maliszewska-Olejniczak K, Kaniowski D, Araszkiewicz M, Tymińska K and Korgul A 2021 Molecular mechanisms of specific cellular DNA damage response and repair induced by the mixed radiation field during boron neutron capture therapy *Front. Oncol.* **11** 676575

Manalad J, Montgomery L and Kildea J 2023 A study of indirect action's impact on simulated neutron-induced DNA damage *Phys. Med. Biol.* **68** 075014

Masunaga S-i, Sanada Y, Tano K, Sakurai Y, Tanaka H, Takata T, Suzuki M and Ono K 2020 An attempt to improve the therapeutic effect of boron neutron capture therapy using commonly employed 10B-carriers based on analytical studies on the correlation among quiescent tumor cell characteristics, tumor heterogeneity and cancer stemness *J. Radiat. Res.* **61** 876–85

McMahon S J, McNamara A L, Schuemann J, Paganetti H and Prise K M 2017 A general mechanistic model enables predictions of the biological effectiveness of different qualities of radiation *Sci. Rep.* **7** 10790

McNamara A, Geng C, Turner R, Mendez J R, Perl J, Held K, Faddegon B, Paganetti H and Schuemann J 2017 Validation of the radiobiology toolkit TOPAS-nBio in simple DNA geometries *Phys. Med.-Eur. J. Med. Phys.* **33** 207–15

McNamara A L *et al* 2018 Geometrical structures for radiation biology research as implemented in the TOPAS-nBio toolkit *Phys. Med. Biol.* **63** 175018

Meylan S, Incerti S, Karamitros M, Tang N, Bueno M, Clairand I and Villagrasa C 2017 Simulation of early DNA damage after the irradiation of a fibroblast cell nucleus using Geant4-DNA *Sci. Rep.* **7** 11923

Michiue H, Sakurai Y, Kondo N, Kitamatsu M, Bin F, Nakajima K, Hirota Y, Kawabata S, Nishiki T-I and Ohmori I 2014 The acceleration of boron neutron capture therapy using multi-linked mercaptoundecahydrododecaborate (BSH) fused cell-penetrating peptide *Biomaterials* **35** 3396–405

Moeini H, Mokari M, Alamatsaz M H and Taleei R 2020 Calculation of the initial DNA damage induced by alpha particles in comparison with protons and electrons using Geant4-DNA *Int. J. Radiat. Biol.* **96** 767–78

Montgomery L, Lund C M, Landry A and Kildea J 2021 Towards the characterization of neutron carcinogenesis through direct action simulations of clustered DNA damage *Phys. Med. Biol.* **66** 205011

Nikjoo H, Emfietzoglou D, Liamsuwan T, Taleei R, Liljequist D and Uehara S 2016 Radiation track, DNA damage and response-a review *Rep. Prog. Phys.* **79** 116601

Nikjoo H, Oneill P, Goodhead D T and Terrissol M 1997 Computational modelling of low-energy electron-induced DNA damage by early physical and chemical events *Int. J. Radiat. Biol.* **71** 467–83

Ochalek T, Nordt F J, Tullberg K and Burger M M 1988 Correlation between cell deformability and metastatic potential in B16-F1 melanoma cell variants *Cancer Res.* **48** 5124–8

Okumura K, Kinashi Y, Kubota Y, Kitajima E, Okayasu R, Ono K and Takahashi S 2013 Relative biological effects of neutron mixed-beam irradiation for boron neutron capture therapy on cell survival and DNA double-strand breaks in cultured mammalian cells *J. Radiat. Res.* **54** 70–5

Probst T U 1999 Methods for boron analysis in boron neutron capture therapy (BNCT). A review *Fresenius' J. Anal. Chem.* **364** 391–403

Qi J, Geng C R, Tang X B, Tian F, Han Y, Liu H, Liu Y H, Bortolussi S and Guan F 2021 Effect of spatial distribution of boron and oxygen concentration on DNA damage induced from boron neutron capture therapy using Monte Carlo simulations *Int. J. Radiat. Biol.* **97** 986–96

Rad A M, Arbab A S, Iskander A, Jiang Q and Soltanian-Zadeh H 2007 Quantification of superparamagnetic iron oxide (SPIO)-labeled cells using MRI *J. Magn. Reson. Imaging* **26** 366–74

Ramos-Mendez J, Perl J, Schuemann J, McNamara A, Paganetti H and Faddegon B 2018 Monte Carlo simulation of chemistry following radiolysis with TOPAS-nBio *Phys. Med. Biol.* **63** 105014

Rodriguez C, Carpano M, Curotto P, Thorp S, Casal M, Juvenal G, Pisarev M and Dagrosa M A 2018 *In vitro* studies of DNA damage and repair mechanisms induced by BNCT in a poorly differentiated thyroid carcinoma cell line *Radiat. Environ. Biophys.* **57** 143–52

Rosenbluth M J, Lam W A and Fletcher D A 2006 Force microscopy of nonadherent cells: a comparison of leukemia cell deformability *Biophys. J.* **90** 2994–3003

Sato T, Masunaga S, Kumada H and Hamada N 2018 Microdosimetric modeling of biological effectiveness for boron neutron capture therapy considering intra- and intercellular heterogeneity in B-10 distribution *Sci. Rep.* **8** 988

Schuemann J, McNamara A L, Ramos-Mendez J, Perl J, Held K D, Paganetti H, Incerti S and Faddegon B 2019 TOPAS-nBio: an extension to the TOPAS simulation toolkit for cellular and sub-cellular radiobiology *Radiat. Res.* **191** 125–38

Sigmund P, Schinner A and Paul H 2009 Errata and addenda for ICRU report 73, stopping of ions heavier than helium *J. ICRU* **5** 1–10 (https://icru.org/wp-content/uploads/2020/12/Errata_and_Addenda_73.pdf)

Small K, Henthorn N, Angal-Kalinin D, Chadwick A, Santina E, Aitkenhead A, Kirkby K J, Smith R, Surman M and Jones J 2021 Evaluating very high energy electron RBE from nanodosimetric pBR322 plasmid DNA damage *Sci. Rep.* **11** 1–12

Stewart R D 2018 Induction of DNA damage by light ions relative to 60Co γ-rays *Int. J. Part. Ther.* **5** 25–39

Tajik M, Rozatian A S and Semsarha F 2015 Simulation of ultrasoft x-rays induced DNA damage using the Geant4 Monte Carlo toolkit *Nucl. Instrum. Methods Phys. Res.* B **342** 258–65

Tang W, Tang B, Li X, Wang Y, Li Z, Gao Y, Gao H, Yan C and Sun L 2021 Cellular S-value evaluation based on real human cell models using the GATE MC package *Appl. Radiat. Isot.* **168** 109509

Warmenhoven J W, Henthorn N T, Ingram S P, Chadwick A L, Sotiropoulos M, Korabel N, Fedotov S, Mackay R I, Kirkby K J and Merchant M J 2020 Insights into the non-homologous end joining pathway and double strand break end mobility provided by mechanistic in silico modelling *DNA Repair* **85** 102743

Webster M, Witkin K L and Cohen-Fix O 2009 Sizing up the nucleus: nuclear shape, size and nuclear-envelope assembly *J. Cell Sci.* **122** 1477–86

Wittig A, Michel J, Moss R L, Stecher-Rasmussen F, Arlinghaus H F, Bendel P, Mauri P L, Altieri S, Hilger R and Salvadori P A 2008 Boron analysis and boron imaging in biological materials for boron neutron capture therapy (BNCT) *Crit. Rev. Oncol./Hematol.* **68** 66–90

Wittig A, Sauerwein W, Coderre J and Coderre J 2000 Mechanisms of transport of p-borono-phenylalanine through the cell membrane *in vitro Radiat. Res.* **153** 173–80